Topological and superconducting properties in bilayer kagome metals YT_6Sn_6 (T=V, Nb, Ta)

Lan-Ting Shi,[1,2,*] Jian-Guo Si,[1,2,*] Akun Liang,[3] Robin Turnbull,[3] Peng-Fei Liu,[1,2] and Bao-Tian Wang[1,2,4,†]

[1]*Institute of High Energy Physics, Chinese Academy of Sciences, Beijing 100049, China*

[2]*Spallation Neutron Source Science Center, Dongguan 523803, China*

[3]*Departamento de Flsica Aplicada-ICMUV-MALTA Consolider Team, Universitat de Valncia, c/Dr. Moliner 50, 46100 Burjassot (Valencia), Spain*

[4]*Collaborative Innovation Center of Extreme Optics, Shanxi University, Taiyuan, Shanxi 030006, China*

(Received 8 December 2022; revised 27 April 2023; accepted 28 April 2023; published 8 May 2023)

Kagome materials exhibit fascinating properties and hold important research significance. Inspired by the extensive studies on the AV_3Sb_5 family of materials, here, we investigate the topological and superconducting properties of the bilayer kagome metal materials YT_6Sn_6 (T=V, Nb, Ta) using first-principles calculations. These kagome materials exhibit the $MgFe_6Ge_6$-prototype structure and have no magnetism. The calculated results for formation energy and the phonon dispersion spectrum demonstrate their stability. Based on the calculation of topologically invariant and surface states, they can be categorized as $\mathbb{Z}_2$ topological metals. The Van Hove singularity and Dirac points are also observed near the Fermi level. According to electron-phonon coupling (EPC) calculations, YT_6Sn_6 systems are all predicted to be weak superconductors. Using the Allen-Dynes modified McMillan formula, the superconducting critical temperatures T_c of YV_6Sn_6, YNb_6Sn_6, and YTa_6Sn_6 are predicted to be 0.65, 1.17, and 0.89 K, respectively. The EPC is mainly contributed by the vibrations of V atoms and partially by the out-of-plane vibrational modes of Sn atoms. The coexistence of nontrivial topological properties and superconducting properties in these bilayer kagome systems is helpful to study the relationship between different physical properties and to design new topological superconductors.

DOI: 10.1103/PhysRevB.107.184503

I. INTRODUCTIONS

Lattice geometry and crystallinity are the key factors in determining the electronic properties of a crystal. One of the most prominent examples is the kagome lattice, which is composed of a two-dimensional corner-sharing triangular network. The kagome lattices of transition metal atoms are a fascinating playground for the exploration of novel correlated and topological electronic phenomena [1–4]. Owing to their intrinsic geometric frustration, kagome systems exhibit a large number of exotic electronic states, such as bond and charge ordering [5–10], chiral superconductivity [9–11], and spin liquid phases [12,13]. The majority of experimental efforts thus far have focused on magnetic systems, such as massive Dirac fermions and flat bands in the ferromagnet Fe_3Sn_2 [14,15] and the antiferromagnet FeSn [16], Chern-gapped Dirac fermions in the ferromagnet $TbMn_6Sn_6$ [17], Weyl fermions in the ferromagnet $Co_3Sn_2S_2$ [18,19], and the noncollinear antiferromagnet Mn_3Sn [20]. The propensity for magnetic order makes certain properties of many existing kagome materials difficult to explore. However, the electronic correlation in the absence of magnetic ordering may be conducive to the emergence of new symmetry-breaking electronic states, which may lead to unusual electronic states in kagome lattices [9–11,21].

Recently, the topological kagome metals AV_3Sb_5 (A = K, Rb, Cs) were discovered by Ortiz *et al.* [22,23]. This family of materials not only possesses a nontrivial topological index [23] but also hosts a cascade of symmetry-breaking electronic orders, including charge density waves (CDWs) [24] and superconductivity [23,25]. Subsequent studies revealed intertwining between these electronic orders, which gives rise to numerous exotic phenomena [26,27], including the intrinsic anomalous Hall effect [28,29], unusual competition between the CDW and superconductivity [30,31], pair density wave order [32,33], and possible Majorana zero modes inside the superconducting vortex core [34]. Although ongoing research indicates a rich interaction between topology and correlation in kagome lattices, the experimental implementation is still limited, mainly due to the scarcity of kagome materials. Therefore, it is important to predict more proportions or species of kagome materials.

Another class of kagome metals is the so-called 166 compounds, which crystallize in the $MgFe_6Ge_6$ prototype structure. The structure has the general chemical formula AB_6X_6, where the A site can accommodate a variety of alkali, alkali earth, and rare earth metals; the B site typically accommodates transition metals; and the X site is typically limited to group IV elements (Si, Ge, Sn). Thus, such materials are chemically diverse. Due to this chemical diversity, the 166 family of materials hosts a wide variety of functionalities, especially in those materials with magnetic order. Examples include the existence of spin-polarized Dirac cones in YMn_6Sn_6 [35], large anomalous Hall effects in $LiMn_6Sn_6$ [36] and

*These authors contributed equally to this work.
†Corresponding author: wangbt@ihep.ac.cn

$GdMn_6Sn_6$ [37], Chern topological magnetism in $TbMn_6Sn_6$ [17], competing magnetic phase in YMn_6Sn_6 [38], catalytic properties in $MgCo_6Ge_6$ [39], negative magnetoresistance in $YMn_6Sn_{6-x}Ga_x$ [40], and a cycloidal spin structure in $HoMn_{6-x}Cr_xGe_6$ [41]. One attraction of the chemical versatility of the 166 compounds is that they can be used to design materials whose magnetic interactions can be modeled independently of the kagome lattice. However, changes in the nonmagnetic *B*-site atoms provide this flexibility and allow the exploration of the interaction between magnetism and kagome-derived band structures. This may induce new electronic phenomena by coupling the triangular lattice plane of the magnetic *A*-site ions with the nonmagnetic *B*-site kagome net. However, nonmagnetic kagome metals are relatively poorly explored relative to their magnetic counterparts. Recent studies of nonmagnetic AV_3Sb_5 compounds [22] showed that abnormal CDW instability and superconductivity can occur when the local magnetic interactions are absent [23,24]. Furthermore, a new class of vanadium-based compounds with kagome bilayers, AV_6Sb_6 ($A=$ K, Rb, Cs), was reported by theoretical calculations combined with angle-resolved photoemission spectroscopy (ARPES) measurements, which reveal that these compounds feature both Dirac nodal lines and pressure-induced superconductivity [42]. Recently, Arachchige *et al.* revealed the CDW modulation in ScV_6Sn_6 using single-crystal x-ray and neutron diffraction [43]. The 166 system materials are also gradually showing characteristics similar to those of the 135 family of materials, especially the electronic-order-related properties guided by the kagome lattice. Therefore, the theoretical prediction of new nonmagnetic kagome metal variants with 166 structure is an attractive topic in this field, which could provide *a priori* guidance for both theory and experiment.

In the present study, we report three bilayer kagome materials, namely, YT_6Sn_6 ($T=$ V, Nb, Ta), where the kagome bilayer is composed of the transition metal V, Nb, or Ta. The crystal structures of the YT_6Sn_6 family of materials are derived from elemental substitution, which is a typical method used to synthesize new materials. For example, $CsAg_5Te_3$ was reported as a thermoelectric material with ultralow thermal conductivity [44]; then $CsCu_5S_3$ [45] and $CsCu_5Se_3$ [46] were successfully prepared with the same crystal structure via elemental substitution. Considering that the AV_3Sb_5 family of materials has rich physical properties, high-throughput calculations were preformed [47,48], and the kagome metals CsM_3Te_5 ($M=$ Ti, Zr, Hf) were predicted to exhibit superconductivity and topological properties [49]. Recently, $CsTi_3Bi_5$ was successfully fabricated with single-crystal structure, and superconductivity was observed [50], which strongly proves the applicability of the element substitution method in kagome families. Here, the stability is determined from thermodynamics and dynamics by calculating the formation energy and phonon spectra. They will likely be synthesized in experiments in the future. The electronic structure shows that the Van Hove singularities and the Dirac points (DPs) appear near the Fermi level without considering the spin-orbit coupling (SOC) effect, and the DPs are gapped when the SOC is turned on. According to calculations of topologically invariant and surface states, YT_6Sn_6 can be categorized as $\mathbb{Z}_2$ topological metals. Their electron-phonon couplings (EPCs) are simulated, and the results show that they are weak superconductors with superconducting critical temperatures around 1 K. It is extremely rare for superconductivity and nontrivial topological properties to coexist in the 166 system, which provides guidance for future theoretical and experimental work to find new topological superconductors, especially in the prototype structure with a bilayer kagome lattice.

II. COMPUTATIONAL DETAILS

Our first-principles calculations of the level of density functional theory (DFT) were conducted using the QUANTUM ESPRESSO package [51]. The ultrasoft pseudopotentials [52] were chosen to describe the interaction between the electrons and ions. The exchange-correlation interaction was described by the generalized gradient approximation and parameterized by the Perdew-Burke-Ernzerhof functional [53]. All calculations used the zero-damping DFT-D3 functional [54] to conduct the van der Waals (vdW) correction accurately. The cutoff energies of the wave functions and charge density were set as 60 and 600 Ry, respectively. All structures were fully relaxed until the Hellmann-Feynman force acting on each atom was less than 10^{-5} Ry/Å, and the convergence criterion for self-consistent calculations was set to be 10^{-6} Ry. The Brillouin zone (BZ) was sampled on a $10\times10\times6$ mesh of **k** points. The surface states were calculated by the iterative Green's function as provided in the WANNIERTOOLS package [55,56], where a tight-binding method based on the maximally localized Wannier function was employed [57,58] while considering the 5*s* orbitals on Y; 5*p* orbitals on Sn; and 3*d*, 4*d*, and 5*d* orbitals on V, Nb, Ta, respectively.

The phonon dispersion curves were calculated based on density functional perturbation theory [59], where a denser $20\times20\times12$ **k**-point grid and a $5\times5\times3$ **q**-point grid were employed for the EPC calculations. The superconducting critical temperature T_c was calculated based on the Allen-Dynes modified McMillan formula [60]:

$$T_c = \frac{\omega_{\log}}{1.2}\exp\left[-\frac{1.04(1+\lambda)}{\lambda-\mu^*-0.62\lambda\mu^*}\right], \tag{1}$$

where μ^* is the effective Coulomb pseudopotential and can be set at a typical value of 0.1. The integrated EPC constant can be evaluated by

$$\lambda(\omega) = 2\int_0^{\omega}\frac{\alpha^2F(\omega')}{\omega'}d\omega'. \tag{2}$$

The EPC constant λ used in Eq. (1) is $\lambda(\omega_{\max})$, where $\omega_{\max}$ is the maximum of the phonon frequency.

Here, $\omega_{\log}$ is the logarithmically averaged characteristic phonon frequency, which is defined as

$$\omega_{\log} = \exp\left[\frac{2}{\lambda}\int\frac{d\omega}{\omega}\alpha^2F(\omega)\ln\omega\right]. \tag{3}$$

The phonon-related calculations were carried out without including the SOC effect because it is less important for describing the vibrational properties [61,62].

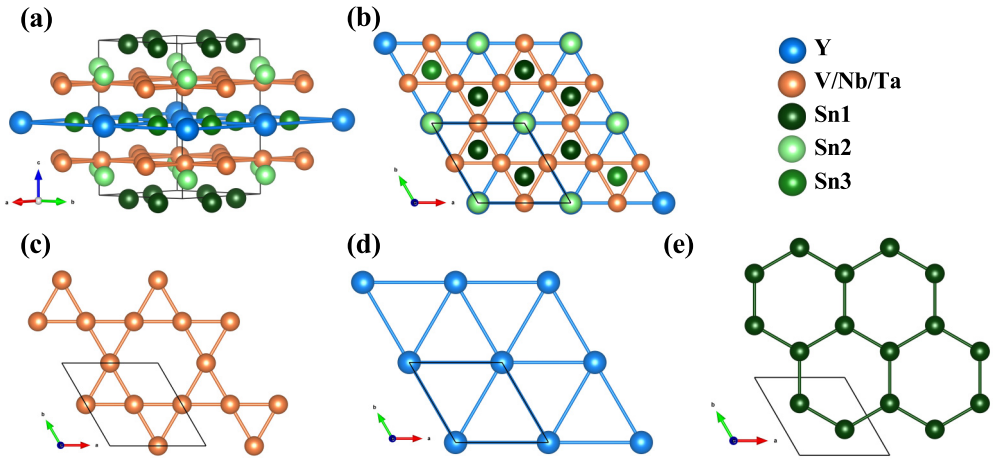

FIG. 1. Crystal structure of YT_6Sn_6 (T = V, Nb, Ta). (a) YT_6Sn_6 lattice structure composed of different layers of YSn3, T3Sn2, and Sn1. (b) Top view of crystal structure looking along the c axis and showing the kagome plane of T atoms and projected Sn1, Sn2, and Sn3 sites. (c) Two-dimensional kagome net of T atoms. (d) Triangular lattice of Y-site ions interwoven in the kagome plane as shown looking along the c axis. (e) Honeycomb layer formed by Sn3 atoms perpendicular to the c axis.

III. RESULTS AND DISCUSSION

A. Crystal structures and thermal stability

Here, we adopt the structure of YV_6Sn_6 as the parent structure, which has been synthesized and confirmed by x-ray single-crystal diffraction data [63]. To predict new materials, we replace the position of V atoms by the family elements Nb and Ta. As shown in Fig. 1, the YT_6Sn_6 crystal structure exhibits different layers along the c axis with a hexagonal space group of $P6/mmm$ (No. 191). There is only one type of Y ion and one type of V/Nb/Ta ion, while the Sn ions occupy three different crystallographic sites denoted by Sn1, Sn2, and Sn3. As shown in Fig. 1(a), the unit cell is composed of four different layers stacked along the c axis, which are formed by Sn1, Sn2, transition metals, and YSn3, respectively. Figure 1(b) reveals the top view of the crystal structure, where the transition metal T atoms form a kagome layer within the ab plane, and the isolated kagome net of T atoms is shown in Fig. 1(c). The Y atoms and Sn2 atoms both form triangular lattice planes, as shown in Fig. 1(d), while the Sn1 and Sn3 atoms form the honeycomb crystal lattices between the two kagome layers of T atoms [see Fig. 1(e)]. When viewed along the c axis, the positions of the Y and Sn2 atoms are aligned, and the positions of the Sn1 and Sn2 are also aligned. It can be seen that although the symmetry of this structure is the same as that of 135 family of materials, the unit structure is quite different, especially the inclusion of the two kagome layers, as well as triangular and hexagonal layers, which may lead to some interesting new properties.

The structural parameters of $P6/mmm$ YT_6Sn_6 after high-accuracy optimizing are shown in Table I. YV_6Sn_6 has the smallest volume, while YNb_6Sn_6 has a slightly larger volume than YTa_6Sn_6. To ascertain the thermodynamic stability of this system, we calculate the formation energy, defined as

$$E_f = \frac{E_{YT_6Sn_6} - E_Y - 6E_T - 6E_{Sn}}{13}. \quad (4)$$

In our calculations, we use $Fm\bar{3}m$ for Y [64], $Fm\bar{3}m$ for V [64], $Im\bar{3}m$ for Nb [65], $Fm\bar{3}m$ for Ta [64], and $Immm$ for Sn [66]. As shown in the last column of Table I, the formation energies of these three structures are all negative, strongly demonstrating their thermodynamic stability and indicating the possibility of experimental synthesis. Moreover, we check the dynamical stability of all proposed structures by calculating the phonon dispersions. As shown in Sec. III C, the absence of phonon modes with imaginary frequencies suggests that the structures are all dynamically stable. It is worth mentioning that the magnetic moments of these systems in different cases are calculated by using the method of nonlinear magnetic moment calculations [67]. The results show that all the magnetic moments are zero. This is consistent with the almost negligible magnetic properties of YV_6Sn_6 measured in experiments [63].

B. Electronic and topological properties

Electronic structure information is the most important way to understand the novel properties of kagome materials. The calculated electronic band structures and density of states (DOS) without considering the SOC effect are shown in Figs. S1 and S2 in the Supplemental Material [68]. Here, we distinguish the energy bands of these system crossing the Fermi level by color; only two bands cross the Fermi level for YV_6Sn_6, and three bands cross the Fermi level for YNb_6Sn_6 and YTa_6Sn_6 (see Fig. 2). As expected, these three kagome compounds show qualitatively similar band structures, where the Dirac-like band-crossing points are located at K points, and this characteristic also exists in the 135 system with kagome structure [25–27]. Increasing the mass of T from V

TABLE I. The crystal parameters and formation energies of YT_6Sn_6.

	a (Å)	c (Å)	E_f (eV)
YV_6Sn_6	5.4260	9.1502	−0.37073
YNb_6Sn_6	5.7330	9.5307	−0.33788
YTa_6Sn_6	5.7038	9.5172	−0.33962

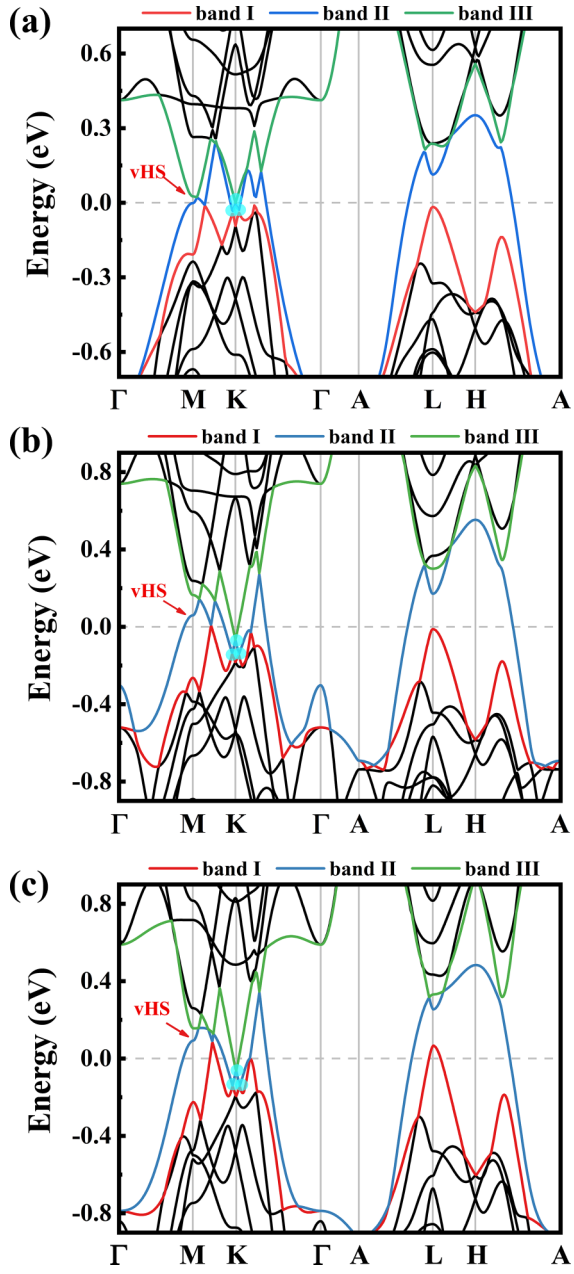

FIG. 2. Band structures without considering the SOC effect for (a) YV_6Sn_6, (b) YNb_6Sn_6, and (c) YTa_6Sn_6. The colored lines indicate the bands crossing the Fermi level. The DPs and the Van Hove singularities are illustrated by the light blue circles and red arrows, respectively. The Fermi level is set to zero.

to Ta, the Dirac cones at the K points move gradually away from the Fermi level, while the Dirac cone of YV_6Sn_6 is just on the Fermi level. In addition, the Van Hove singularity is detected at the M point. Similarly, the Van Hove singularity of YV_6Sn_6 is located at the Fermi level, and others move up with an increasing mass of T atoms. Such phenomena are typical characteristics in the band structure of kagome materials [63]. The calculated electronic DOS (on the right in Figs. S1 and S2) clearly shows that most electrons near the Fermi level of this system are provided by the d electrons of the transition metal atoms.

The AV_3Sb_5 family of materials was repeatedly reported as being topological metals [69] through analyses of the parity of the wave function at the time reversal invariant momentum (TRIM) points and the surface states. Here, we also investigate the topological properties. Figures 3(a)–3(c) show the band structures of YT_6Sn_6 with the SOC effect switched on. Interestingly, for the bands near the Fermi level, two continuous band gaps are formed across the whole BZ at the Fermi level after the SOC effect is included, which is consistent with the report by Pokharel *et al.* [63]. It can be seen that the SOC effects are significantly enhanced with the increase of the atomic mass of the transition metals, and the Van Hove singularities are robust, existing at the M point. For YV_6Sn_6, the Dirac-like band-crossing points are gapped about 27 meV. With increasing mass of the T atom, the gaps at the K point are enhanced to 27.2 and 112 meV for YNb_6Sn_6 and YTa_6Sn_6, respectively. Furthermore, the gaps at the $\Gamma(A)$ points are opened to 53.4 (17.9) and 117.2 (122.6) meV for YV_6Sn_6 and YTa_6Sn_6, respectively. However, for YNb_6Sn_6, the gap at the A point is enhanced 119.9 meV with the inclusion of SOC.

Similar to the kagome metals CsV_3Sb_5 [69] and GdV_6Sn_6 [63], the YT_6Sn_6 family of materials exhibits both inversion and time reversal symmetries. Given the continuous band gaps across the whole BZ, we can calculate the $\mathbb{Z}_2$ indices of each band around the Fermi level by analyzing the parity of the wave function at the eight TRIM points [69–71]. The calculated results are listed in Table II. The topological invariant $\mathbb{Z}_2 = 1$ can be assigned to band II of YV_6Sn_6 and YNb_6Sn_6 and bands II and III of YTa_6Sn_6. These results indicate that the materials in the YT_6Sn_6 family all exhibit topologically nontrivial characteristics.

For a traditional hexagonal structure, the BZ can be classified into unequal cases: namely, the top (001) plane, which is the easy cleavage surface due to the vdW interaction between layers, and the side (100) plane, as shown in Fig. S3. Here, we calculate the surface states of these two planes. Many obvious surface states, which are not present in the bulk, can be identified near the Fermi level [see Figs. 3(d)–3(f) and S4]. This feature can be easily observed in the ARPES measurements. It can be seen that the gaps in the surface states gradually increase with increasing atomic mass of the transition metal, agreeing well with the band structure calculations. Near the Fermi level, the surface bands can be seen emitting from the bulk Dirac cones on either side, which was also found in the study of YV_6Sn_6 and GdV_6Sn_6 [63]. As a consequence, the characteristics of topological nontrivial surface states and the continuous band gaps make it easy to define the YT_6Sn_6 family as $\mathbb{Z}_2$ topological metals.

C. Phonon vibrations properties

To better understand the phonon vibrations properties of YT_6Sn_6, we project the weights of different atomic vibration modes on the phonon dispersion curve and also calculate the phonon density of states (see Fig. 4). The absence of the imaginary modes clearly indicates that these materials are dynamically stable. Obviously, the vibrations of the three types atoms (Y, T, Sn) in these materials are gradually coupled together as the mass of the transition metal atoms constituting the kagome layer changes.

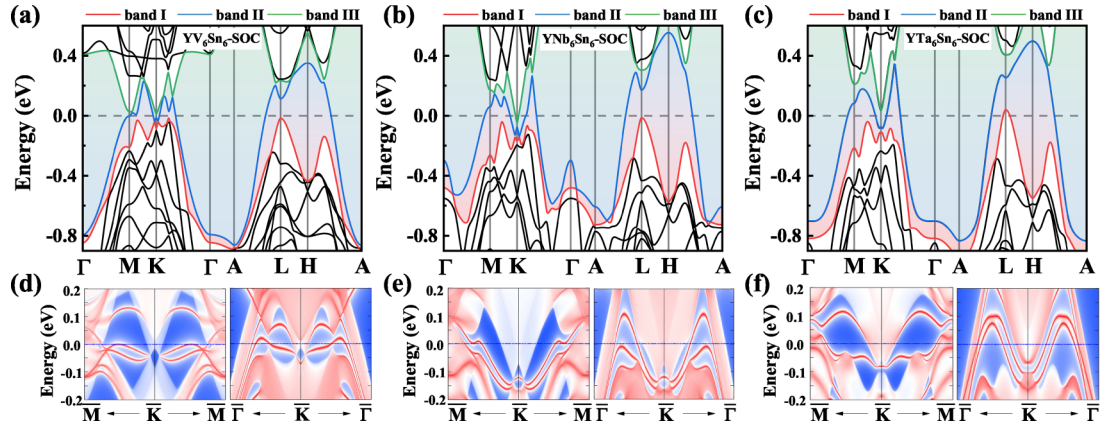

FIG. 3. Band structures calculated including the SOC effect for (a) YV_6Sn_6, (b) YNb_6Sn_6, and (c) YTa_6Sn_6. The colored lines indicate the bands crossing the Fermi level, and the colored shading illustrates the continuous band gaps in the BZ. Surface states on the (001) surface of (d) YV_6Sn_6, (e) YNb_6Sn_6, and (f) YTa_6Sn_6 are also illustrated. The Fermi level is set to zero.

For YV_6Sn_6, the vibrations of the three atoms are relatively separated. The vibrations of the V atoms are located in the high-frequency region (175–325 cm^{-1}), and the vibration frequency in the direction perpendicular to the kagome layer is higher than that in the parallel direction. The vibrations of the Y atoms are located in the intermediate-frequency region (175–200 cm^{-1}). The vibrations of Sn atoms are in the low-frequency region (0–175 cm^{-1}). However, for YNb_6Sn_6 [see Fig. 4(b)], the phonon vibrations of Nb atoms in different directions are coupled, and the vibrations of Y atoms in two directions are completely split. Interestingly, the vibrations of Sn atoms spread to the high-frequency region, especially the vibrations in the z direction. In addition, the acoustic branch dominated by the vibrations of Sn atoms in the z direction shows significant softening, which may contribute to the enhancement of its EPC strength [72]. For YTa_6Sn_6, the phonon vibrations of the Ta atoms are located in the intermediate-frequency region, and the vibrations of the Sn atoms cover almost the entire frequency range.

Interestingly, we find that the in-plane (xy direction) and out-of-plane (z direction) vibrations of different atoms have different degrees of splitting or mixing. The two vibrational modes of the Y atom are almost completely mixed in YV_6Sn_6 but are nearly split in YNb_6Sn_6 and are partially mixed in YTa_6Sn_6. The vibrational modes of the transition metal atoms in the z direction are more discrete with the increase of mass, and the two vibrational modes transform from the splitting of V to the mixing of Ta. However, the vibrations of the Sn atoms are opposite to those of the transition metal atoms, and the vibrations in the z direction are split in the high-frequency region with the increase of the mass of T.

To check whether the CDW transition happens in YT_6Sn_6 (T = V, Nb, Ta), we recalculate the phonon dispersion by changing the Fermi-Dirac smearing factor σ. This parameter takes on a physical meaning to directly reflect the electronic temperature of the system [73]. We can see that the character of absence of imaginary frequency is robust for YV_6Sn_6 and YTa_6Sn_6 from Fig. S5, indicating the systems are stable with a high-symmetry phase and will not undergo any CDW transitions. For YNb_6Sn_6, there is a stiff imagery mode at the A point, while a very small smearing parameter (σ = 0.001 Ry) is used. It gradually disappears with the increase of the smearing parameter σ. Such phenomena demonstrate that only YNb_6Sn_6 may experience a CDW transition with decreasing temperature, just like the case of ScV_6Sn_6 [43].

D. Superconductivity properties

The phonon dispersions weighted by the magnitude of the phonon linewidth $\gamma_{\mathbf{q}\upsilon}$, the Eliashberg electron-phonon

TABLE II. Parity of the wave function at TRIM points and the $\mathbb{Z}_2$ indices of YT_6Sn_6.

		Parity				Product of parity				
	Band index	Γ	3M	A	3L	Γ	3M	A	3L	$\mathbb{Z}_2$
YV_6Sn_6	I	+	−	+	+	+	−	−	+	0
	II	+	−	−	−	+	+	+	−	1
	III	−	−	−	+	−	−	−	−	0
YNb_6Sn_6	I	+	+	−	+	+	−	+	+	1
	II	+	−	+	−	+	+	+	−	1
	III	−	−	−	+	−	−	−	−	0
YTa_6Sn_6	I	+	+	−	+	+	−	−	+	0
	II	+	−	−	−	+	+	+	−	1
	III	−	+	−	+	−	+	−	−	1

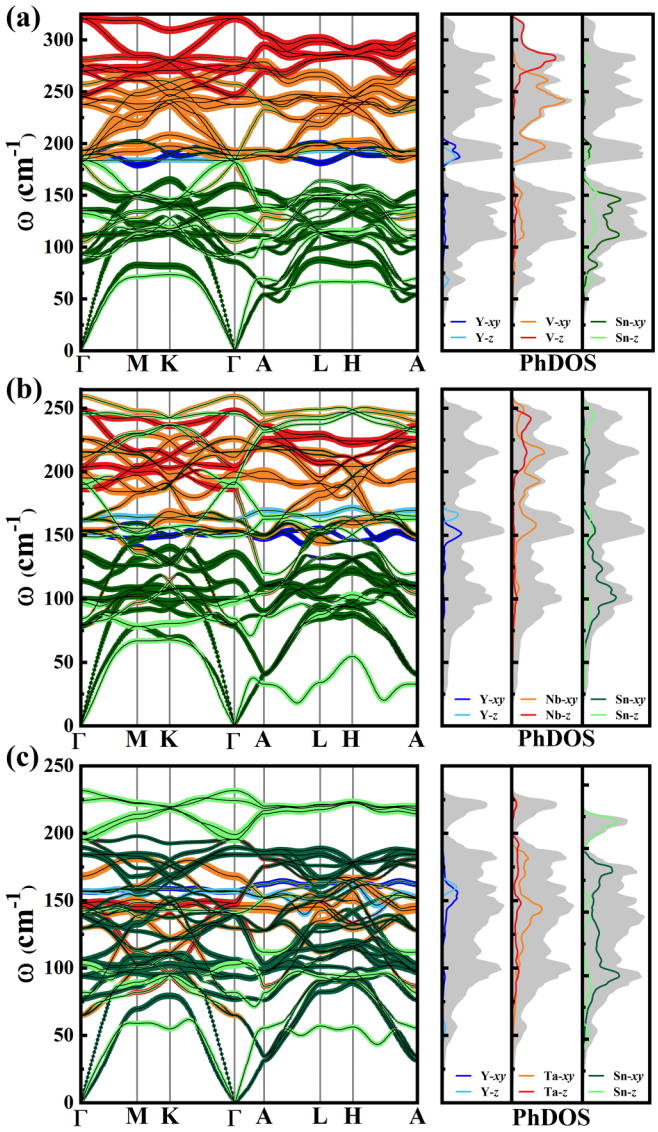

FIG. 4. Phonon dispersions weighted by different atomic vibrational modes as well as the total (gray-shaded zone) and vibrational mode-resolved (colored lines) phonon density of states of (a) YV_6Sn_6, (b) YNb_6Sn_6, and (c) YTa_6Sn_6.

spectral function $\alpha^2F(\omega)$, and the cumulative frequency dependence of EPC λ are illustrated in Fig. 5. Here, the phonon linewidth can be estimated by

$$\gamma_{\mathbf{qv}} = 2\pi\omega_{\mathbf{qv}} \sum_{ij} \int \frac{d^3k}{\Omega_{\mathrm{BZ}}} |g_{\mathbf{qv}}(k,i,j)|^2 \times \delta(\varepsilon_{\mathbf{q},i} - \varepsilon_F)\delta(\varepsilon_{k+\mathbf{q},j} - \varepsilon_F), \quad (5)$$

where Ω_{BZ} is the volume of the BZ, $\varepsilon_{\mathbf{q},i}$ and $\varepsilon_{k+\mathbf{q},j}$ denote the Kohn-Sham energies, and $g_{\mathbf{qv}}(k,i,j)$ represents the EPC matrix element [60]. $g_{\mathbf{qv}}(k,i,j)$, which can be determined self-consistently using the linear response theory, describes the probability amplitude for the scattering of an electron with a transfer of crystal momentum $\mathbf{q}$ [60]. It is worthwhile to recall that $\gamma_{\mathbf{q}v}$ reflects the EPC contribution, which does not depend on the real or imaginary character of the phonon frequency [74].

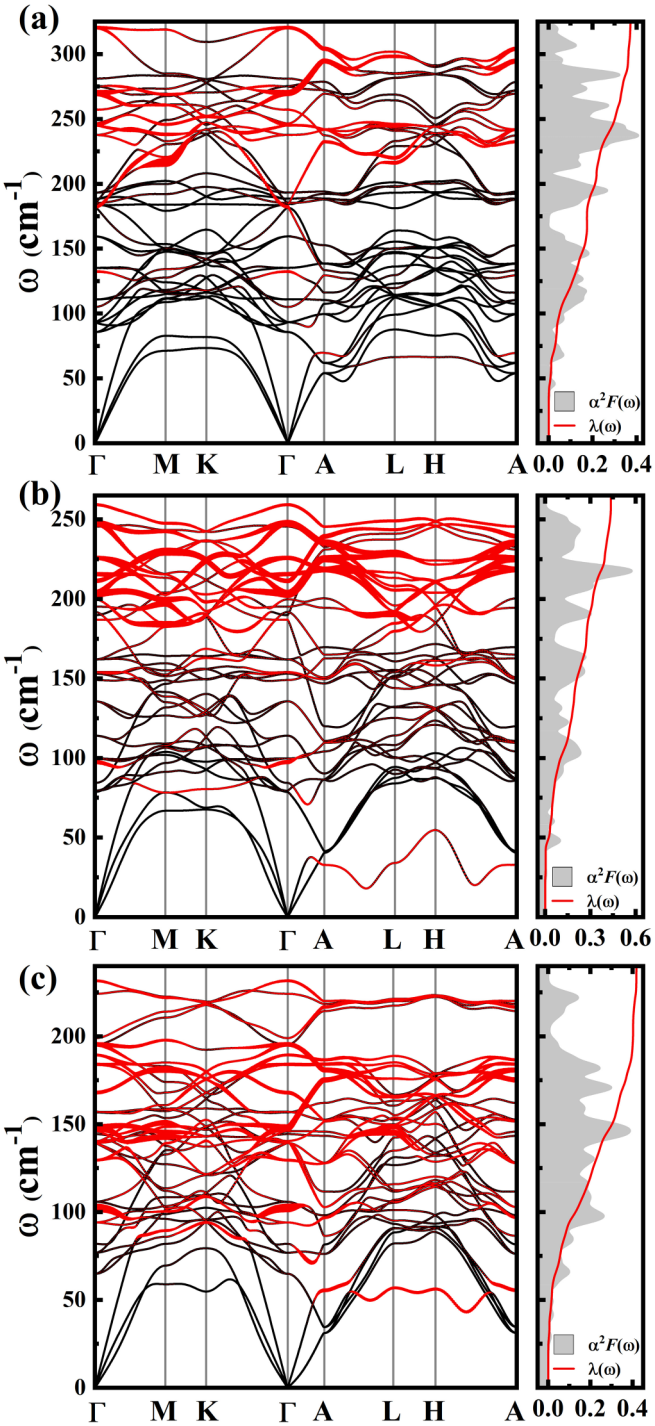

FIG. 5. (a) Phonon dispersions weighted by the magnitude of the phonon linewidth (red circles) for YV_6Sn_6. The right panel indicates the Eliashberg spectral function $\alpha^2F(\omega)$ (gray shading) and the integrated strength of EPC of $\lambda(\omega)$ (red line). (b) and (c) The same as (a), but for YNb_6Sn_6 and YTa_6Sn_6, respectively.

From Fig. 5, it is clear that the main contribution to the phonon linewidth (and consequently to the EPC) arises from the vibration of V atoms in the high-energy phonon bands, with a small contribution from the vibrations of Sn in the z direction in the intermediate-frequency region for YV_6Sn_6. Similarly, for YNb_6Sn_6 and YTa_6Sn_6, the vibrations of the

TABLE III. Calculated total EPC parameter λ, logarithmic average phonon frequency $\omega_{\log}$, and superconductivity transition temperatures T_c of YT_6Sn_6.

	λ	$\omega_{\log}$	T_c (K)
YV_6Sn_6	0.373	238.632	0.65
YNb_6Sn_6	0.429	192.388	1.17
YTa_6Sn_6	0.418	166.476	0.89

transition metal atoms in the high-frequency region play a critical role in the phonon linewidth. The contribution from out-of-plane vibrations of Sn atoms increases gradually in the intermediate-frequency region. It is noteworthy that a distinct soft mode appears on an acoustic branch for these two materials, and the phonon linewidth of this soft mode is mainly contributed by the out-of-plane vibrations of Sn atoms. This EPC-caused soft mode may be attributed to the Kohn anomalies and further induce a CDW transition with some perturbation in experiment, such as a decrease in temperature. This result is consistent with recent studies of a material in the same system, ScV_6Sn_6 [43], which shows Sn atoms cause the CDW order.

The calculated total EPC parameter λ, logarithmic average phonon frequency $\omega_{\log}$, and superconductivity transition temperatures T_c of YT_6Sn_6 are listed in Table III. The total λ for YV_6Sn_6, YNb_6Sn_6, and YTa_6Sn_6 are calculated to be 0.373, 0.429, and 0.418, respectively. Thus, this family of materials can be classified as weak superconductors under ambient conditions. Taking the $\lambda(\omega_{\max})$ and $\omega_{\log}$ into Eq. (1), we can obtain their superconducting critical temperature T_c. The simulated T_c for YV_6Sn_6, YNb_6Sn_6, and YTa_6Sn_6 are 0.65, 1.17, and 0.89 K, respectively. It can clearly be seen that T_c of these bilayer kagome materials are positively correlated with the EPC constant λ, indicating that these systems are traditional phonon-mediated superconductors. In addition, we check the influence of the Coulomb potential μ^* on the superconductivity critical temperature T_c. As shown in Fig. S6, the T_c values of all three materials decrease with increasing μ^*. When $\mu^* = 0$, T_c of YV_6Sn_6, YNb_6Sn_6, and YTa_6Sn_6 can reach 4.26, 5.01, and 4.17 K, and the T_c values tend to be close to zero as μ^* increases to 0.2. Considering that the traditional 166 systems always exhibit fantastic magnetic orders [35,38,40,41,75], the YT_6Sn_6 system breaks this rule and can be claimed to be weak superconductors. Therefore, our results provide a good opportunity to explore the novel properties in the 166 kagome system.

IV. CONCLUSIONS

In conclusion, we systematically investigated the topological and superconducting properties of the bilayer kagome materials YT_6Sn_6 (T = V, Nb, Ta) by using first-principles calculations. The results for the formation energy and phonon dispersion confirm their thermodynamic and dynamic stability. At the M point in the BZ, the Van Hove singularity appears robustly near the Fermi level. Without considering the SOC effect, the band structures show several Dirac-liked band-crossing points near the Fermi level. After including SOC, the DPs are gapped, and two continuous band gaps form. The surface states on the (001) surface in the valence bands and the topologically nontrivial nature clearly indicate that the YT_6Sn_6 kagome materials are topological metals. By analytically solving the McMillan-Allen-Dynes formula derived from the microscopic theory of BCS, we predicted that YT_6Sn_6 materials are weak EPC superconductors. The EPC is mainly contributed by the vibrations of V atoms and the out-of-plane vibrations of Sn. The coexistence of superconductivity and nontrivial band structure suggests that these three bilayer kagome materials are all promising candidates for the study of topological superconductivity. Our findings provide a platform for exploring the relationship between superconductivity and topological states in the family of kagome lattices.

ACKNOWLEDGMENTS

The authors gratefully acknowledge financial support from the National Natural Science Foundation of China (Grants No. 12104458 and No. 12074381) and the Guangdong Basic and Applied Basic Research Foundation (Grant No. 2022A1515110404). The authors also acknowledge the computational resources from the Supercomputer Centre of the China Spallation Neutron Source. R.T. thanks the Generalitat Valenciana for Postdoctoral Fellowship No. CIAPOS/2021/20.

[1] S. Sachdev, Phys. Rev. B **45**, 12377 (1992).
[2] H. M. Guo and M. Franz, Phys. Rev. B **80**, 113102 (2009).
[3] I. I. Mazin, H. O. Jeschke, F. Lechermann, H. Lee, M. Fink, R. Thomale, and R. Valenti, Nat. Commun. **5**, 4261 (2014).
[4] T. Bilitewski and R. Moessner, Phys. Rev. B **98**, 235109 (2018).
[5] X. Plat, F. Alet, S. Capponi, and K. Totsuka, Phys. Rev. B **92**, 174402 (2015).
[6] J. Wen, A. Rüegg, C.-C. J. Wang, and G. A. Fiete, Phys. Rev. B **82**, 075125 (2010).
[7] S. V. Isakov, S. Wessel, R. G. Melko, K. Sengupta, and Y. B. Kim, Phys. Rev. Lett. **97**, 147202 (2006).
[8] H. C. Jiang, T. Devereaux, and S. A. Kivelson, Phys. Rev. Lett. **119**, 067002 (2017).
[9] M. L. Kiesel, C. Platt, and R. Thomale, Phys. Rev. Lett. **110**, 126405 (2013).
[10] W.-S. Wang, Z.-Z. Li, Y.-Y. Xiang, and Q.-H. Wang, Phys. Rev. B **87**, 115135 (2013).
[11] S.-L. Yu and J.-X. Li, Phys. Rev. B **85**, 144402 (2012).
[12] L. Balents, M. P. A. Fisher, and S. M. Girvin, Phys. Rev. B **65**, 224412 (2002).
[13] S. Yan, D. A. Huse, and S. R. White, Science **332**, 1173 (2011).
[14] L. Ye, M. Kang, J. Liu, F. von Cube, C. R. Wicker, T. Suzuki, C. Jozwiak, A. Bostwick, E. Rotenberg, D. C. Bell, L. Fu, R. Comin, and J. G. Checkelsky, Nature (London) **555**, 638 (2018).

[15] Z. Lin, J. H. Choi, Q. Zhang, W. Qin, S. Yi, P. Wang, L. Li, Y. Wang, H. Zhang, Z. Sun, L. Wei, S. Zhang, T. Guo, Q. Lu, J. H. Cho, C. Zeng, and Z. Zhang, Phys. Rev. Lett. **121**, 096401 (2018).

[16] M. Kang *et al.*, Nat. Mater. **19**, 163 (2020).

[17] J. X. Yin *et al.*, Nature (London) **583**, 533 (2020).

[18] E. Liu *et al.*, Nat. Phys. **14**, 1125 (2018).

[19] D. F. Liu, A. J. Liang, E. K. Liu, Q. N. Xu, Y. W. Li, C. Chen, D. Pei, W. J. Shi, S. K. Mo, P. Dudin, T. Kim, C. Cacho, G. Li, Y. Sun, L. X. Yang, Z. K. Liu, S. S. P. Parkin, C. Felser, and Y. L. Chen, Science **365**, 1282 (2019).

[20] K. Kuroda *et al.*, Nat. Mater. **16**, 1090 (2017).

[21] W.-H. Ko, P. A. Lee, and X.-G. Wen, Phys. Rev. B **79**, 214502 (2009).

[22] B. R. Ortiz, L. C. Gomes, J. R. Morey, M. Winiarski, M. Bordelon, J. S. Mangum, I. W. H. Oswald, J. A. Rodriguez-Rivera, J. R. Neilson, S. D. Wilson, E. Ertekin, T. M. McQueen, and E. S. Toberer, Phys. Rev. Mater. **3**, 094407 (2019).

[23] B. R. Ortiz, S. M. L. Teicher, Y. Hu, J. L. Zuo, P. M. Sarte, E. C. Schueller, A. M. M. Abeykoon, M. J. Krogstad, S. Rosenkranz, R. Osborn, R. Seshadri, L. Balents, J. He, and S. D. Wilson, Phys. Rev. Lett. **125**, 247002 (2020).

[24] Y.-X. Jiang *et al.*, Nat. Mater. **20**, 1353 (2021).

[25] B. R. Ortiz, P. M. Sarte, E. M. Kenney, M. J. Graf, S. M. L. Teicher, R. Seshadri, and S. D. Wilson, Phys. Rev. Mater. **5**, 034801 (2021).

[26] K. Jiang, T. Wu, J.-X. Yin, Z. Wang, M. Z. Hasan, S. D. Wilson, X. Chen, and J. Hu, Nat. Sci. Rev. **10**, nwac199 (2023).

[27] J.-G. Si, W.-J. Lu, Y.-P. Sun, P.-F. Liu, and B.-T. Wang, Phys. Rev. B **105**, 024517 (2022).

[28] S.-Y. Yang, Y. Wang, B. R. Ortiz, D. Liu, J. Gayles, E. Derunova, R. Gonzalez-Hernandez, L. Šmejkal, Y. Chen, S. S. P. Parkin, S. D. Wilson, E. S. Toberer, T. McQueen, and M. N. Ali, Sci. Adv. **6**, eabb6003 (2020).

[29] F. H. Yu, T. Wu, Z. Y. Wang, B. Lei, W. Z. Zhuo, J. J. Ying, and X. H. Chen, Phys. Rev. B **104**, L041103 (2021).

[30] F. H. Yu, D. H. Ma, W. Z. Zhuo, S. Q. Liu, X. K. Wen, B. Lei, J. J. Ying, and X. H. Chen, Nat. Commun. **12**, 3645 (2021).

[31] K. Y. Chen, N. N. Wang, Q. W. Yin, Y. H. Gu, K. Jiang, Z. J. Tu, C. S. Gong, Y. Uwatoko, J. P. Sun, H. C. Lei, J. P. Hu, and J. G. Cheng, Phys. Rev. Lett. **126**, 247001 (2021).

[32] H. Zhao, H. Li, B. R. Ortiz, S. M. L. Teicher, T. Park, M. Ye, Z. Wang, L. Balents, S. D. Wilson, and I. Zeljkovic, Nature (London) **599**, 216 (2021).

[33] H. Chen *et al.*, Nature (London) **599**, 222 (2021).

[34] Z. Liang, X. Hou, F. Zhang, W. Ma, P. Wu, Z. Zhang, F. Yu, J. J. Ying, K. Jiang, L. Shan, Z. Wang, and X. H. Chen, Phys. Rev. X **11**, 031026 (2021).

[35] M. Li, Q. Wang, G. Wang, Z. Yuan, W. Song, R. Lou, Z. Liu, Y. Huang, Z. Liu, H. Lei, Z. Yin, and S. Wang, Nat. Commun. **12**, 3129 (2021).

[36] D. Chen, C. Le, C. Fu, H. Lin, W. Schnelle, Y. Sun, and C. Felser, Phys. Rev. B **103**, 144410 (2021).

[37] T. Asaba, S. M. Thomas, M. Curtis, J. D. Thompson, E. D. Bauer, and F. Ronning, Phys. Rev. B **101**, 174415 (2020).

[38] N. J. Ghimire, R. L. Dally, L. Poudel, D. C. Jones, D. Michel, N. T. Magar, M. Bleuel, M. A. McGuire, J. S. Jiang, J. F. Mitchell, J. W. Lynn, and I. I. Mazin, Sci. Adv. **6**, eabe2680 (2020).

[39] C. Gieck, M. Schreyer, T. F. Fassler, S. Cavet, and P. Claus, Chem. Eur. J. **12**, 1924 (2006).

[40] S.-Y. Zhang, P. Zhao, Z.-H. Cheng, R.-W. Li, J.-Rr. Sun, H.-W. Zhang, and B.-G. Shen, Phys. Rev. B **64**, 212404 (2001).

[41] P. Schobinger-Papamantellos, J. Rodrłguez-Carvajal, and K. H. J. Buschow, J. Magn. Magn. Mater. **408**, 233 (2016).

[42] M. Shi, F. Yu, Y. Yang, F. Meng, B. Lei, Y. Luo, Z. Sun, J. He, R. Wang, Z. Jiang, Z. Liu, D. Shen, T. Wu, Z. Wang, Z. Xiang, J. Ying, and X. Chen, Nat. Commun. **13**, 2773 (2022).

[43] H. W. S. Arachchige, W. R. Meier, M. Marshall, T. Matsuoka, R. Xue, M. A. McGuire, R. P. Hermann, H. Cao, and D. Mandrus, Phys. Rev. Lett. **129**, 216402 (2022).

[44] H. Lin, G. Tan, J. N. Shen, S. Hao, L. M. Wu, N. Calta, C. Malliakas, S. Wang, C. Uher, C. Wolverton, and M. G. Kanatzidis, Angew. Chem., Int. Ed. **55**, 11431 (2016).

[45] N. Ma, F. Jia, L. Xiong, L. Chen, Y. Y. Li, and L. M. Wu, Inorg. Chem. **58**, 1371 (2019).

[46] N. Ma, Y. Y. Li, L. Chen, and L. M. Wu, J. Am. Chem. Soc. **142**, 5293 (2020).

[47] Y. Jiang, Z. Yu, Y. Wang, T. Lu, S. Meng, K. Jiang, and M. Liu, Chin. Phys. Lett. **39**, 047402 (2022).

[48] X.-W. Yi, X.-Y. Ma, Z. Zhang, Z.-W. Liao, J.-Y. You, and G. Su, Phys. Rev. B **106**, L220505 (2022).

[49] J.-G. Si, L.-T. Shi, P.-F. Liu, P. Zhang, and B.-T. Wang, Phys. Rev. B **106**, 214527 (2022).

[50] H. Yang, Y. Ye, Z. Zhao, J. Liu, X.-W. Yi, Y. Zhang, J. Shi, J.-Y. You, Z. Huang, and B. J. Wang, arXiv:2211.12264.

[51] P. Giannozzi *et al.*, J. Phys.: Condens. Matter **21**, 395502 (2009).

[52] D. Vanderbilt, Phys. Rev. B **41**, 7892 (1990).

[53] J. P. Perdew, K. Burke, and M. Ernzerhof, Phys. Rev. Lett. **77**, 3865 (1996).

[54] S. Grimme, J. Antony, S. Ehrlich, and H. Krieg, J. Chem. Phys. **132**, 154104 (2010).

[55] M. P. L. Sancho, J. M. L. Sancho, J. M. L. Sancho, and J. Rubio, J. Phys. F **15**, 851 (1985).

[56] Q. Wu, S. Zhang, H.-F. Song, M. Troyer, and A. A. Soluyanov, Comput. Phys. Commun. **224**, 405 (2018).

[57] I. Souza, N. Marzari, and D. Vanderbilt, Phys. Rev. B **65**, 035109 (2001).

[58] N. Marzari, A. A. Mostofi, J. R. Yates, I. Souza, and D. Vanderbilt, Rev. Mod. Phys. **84**, 1419 (2012).

[59] S. Baroni, S. de Gironcoli, A. D. Corso, and P. Giannozzi, Rev. Mod. Phys. **73**, 515 (2001).

[60] P. B. Allen and R. C. Dynes, Phys. Rev. B **12**, 905 (1975).

[61] B.-T. Wang, P. Zhang, R. Lizárraga, I. Di Marco, and O. Eriksson, Phys. Rev. B **88**, 104107 (2013).

[62] L. Yan, B. T. Wang, X. Huang, Q. Li, K. Xue, J. Zhang, W. Ren, and L. Zhou, Nanoscale **13**, 18947 (2021).

[63] G. Pokharel, S. M. L. Teicher, B. R. Ortiz, P. M. Sarte, G. Wu, S. Peng, J. He, R. Seshadri, and S. D. Wilson, Phys. Rev. B **104**, 235139 (2021).

[64] J. Häglund, A. Fernández Guillermet, G. Grimvall, and M. Körling, Phys. Rev. B **48**, 11685 (1993).

[65] H. G. Schimmel, J. Huot, L. C. Chapon, F. D. Tichelaar, and F. M. Mulder, J. Am. Chem. Soc. **127**, 14348 (2005).

[66] W. J. Helfrich and R. A. Dodd, Acta Metall. **12**, 667 (1964).

[67] J. T. Haraldsen and R. S. Fishman, J. Phys.: Condens. Matter **21**, 216001 (2009).

[68] See Supplemental Material at http://link.aps.org/supplemental/10.1103/PhysRevB.107.184503 for additional figures.

[69] H. Tan, Y. Liu, Z. Wang, and B. Yan, Phys. Rev. Lett. **127**, 046401 (2021).

[70] T. Machida, Y. Sun, S. Pyon, S. Takeda, Y. Kohsaka, T. Hanaguri, T. Sasagawa, and T. Tamegai, Nat. Mater. **18**, 811 (2019).

[71] X. H. Tu, P. F. Liu, W. Yin, J. R. Zhang, P. Zhang, and B. T. Wang, Mater. Today Phys. **24**, 100674 (2022).

[72] L.-T. Shi, R. Turnbull, A. Liang, X.-R. Chen, and G.-F. Ji, J. Mater. Chem. C **10**, 3081 (2022).

[73] D. L. Duong, M. Burghard, and J. C. Schön, Phys. Rev. B **92**, 245131 (2015).

[74] Y. Liu, D. F. Shao, L. J. Li, W. J. Lu, X. D. Zhu, P. Tong, R. C. Xiao, L. S. Ling, C. Y. Xi, L. Pi, H. F. Tian, H. X. Yang, J. Q. Li, W. H. Song, X. B. Zhu, and Y. P. Sun, Phys. Rev. B **94**, 045131 (2016).

[75] G. Venturini, B. C. E. Idrissi, and B. Malaman, J. Magn. Magn. Mater. **94**, 35 (1991).